Intracellular Chemical Imaging of Heme-Containing Enzymes Involved in Innate Immunity Using Resonance Raman Microscopy

Henk-Jan van Manen,*,† Yvonne M. Kraan,† Dirk Roos,‡ and Cees Otto†

Biophysical Engineering Group, Faculty of Science & Technology, University of Twente, P.O. Box 217, 7500 AE Enschede, The Netherlands, and Department of Experimental Immunohematology, Sanquin Research, and Landsteiner Laboratory, Academic Medical Centre, University of Amsterdam, Plesmanlaan 125, 1066 CX Amsterdam, The Netherlands

Vibrational microspectroscopy has become a powerful tool in cellular biology because detailed information about the chemical composition of subcellular, femtoliter volumes can be obtained. Moreover, biological imaging techniques based on this type of spectroscopy avoid labeling methods and artifacts arising from them because the required contrast is generated from endogenous molecules. Here, we report the visualization, by confocal Raman microscopy, of the intracellular distribution of two enzymes important in the immune response of granulocytes (i.e., the NADPH oxidase subunit cytochrome b_{558} (cyt b_{558}) in neutrophils and eosinophil peroxidase (EPO) in eosinophils). We excited these leukocytes with 413.1 nm laser light, allowing the Raman scattering signal from the heme-containing enzymes to be dramatically enhanced by resonance. In neutrophils, there is a nonnegligible contribution from the hemoprotein myeloperoxidase to the resonance Raman signal. The effect of photobleaching of the Raman signal at 413.1 nm excitation on the reconstructed Raman images is discussed. We also show how singular value decomposition can significantly reduce the noise that is present in the raw spectral data. Stimulation of the neutrophils, either by phagocytosis or by phorbol 12-myristate 13-acetate (PMA), resulted in intracellular redistributions of cyt b_{558}. Spectra extracted from Raman images of PMA-activated neutrophils displayed a significantly higher level of cyt b_{558} reduction than spectra from resting neutrophils, indicating that cyt b_{558} reduction is linked with NADPH oxidase activation. The versatility of resonance Raman microscopy on leukocytes is further demonstrated by the visualization of EPO in single eosinophils. In conclusion, high-resolution cellular imaging based on resonance Raman spectroscopy enables the label-free visualization of the intracellular distribution of cyt b_{558} in neutrophils and EPO in eosinophils, two crucial enzymes in leukocyte innate immunity.

Introduction

Among leukocytes, the professional phagocytes (neutrophils, eosinophils, and macrophages) are the effector cells of the innate immune response. Whereas neutrophils and macrophages are responsible for the degradation and killing of invading microorganisms such as bacteria and fungi, eosinophils are involved in parasite destruction. Upon activation, all of these phagocytes employ an intricate enzyme complex known as NADPH oxidase to generate superoxide (O_2^-) from oxygen in a process called the respiratory burst.[1] Subsequently, a cocktail of highly reactive and microbicidal species is poured inside the phagosome or released extracellularly. This mixture contains reactive oxygen species (ROS)[1] derived from superoxide (e.g., hydrogen peroxide, hydroxyl radicals, singlet oxygen, and hypochlorous acid) and also proteases such as elastase and cathepsin G that are released from granules.[2] Hypochlorous acid is produced from hydrogen peroxide by myeloperoxidase (MPO), an abundant neutrophilic enzyme that is also released from primary granules.[3]

Numerous studies have dealt with the elucidation of the molecular mechanism that underlies the production of superoxide by NADPH oxidase.[1] The catalytic core of NADPH oxidase is formed by cytochrome b_{558} (cyt b_{558}), a heterodimeric membrane protein consisting of gp91^{phox} and p22^{phox}. The glycosylated subunit gp91^{phox} is a flavohemoprotein containing all of the catalytically active parts. Electrons are transferred from NADPH to oxygen via a bound flavin adenine dinucleotide (FAD) and two hemes embedded in transmembrane helices. The small subunit p22^{phox} is a stabilizing protein for gp91^{phox} and a docking site for cytosolic proteins that are indispensable for in vivo NADPH oxidase activation.[1,4] The architecture of NADPH oxidase (i.e., the separation between membrane-bound and cytosolic subunits) allows its activity to be tightly regulated. This is crucial, because accidental or excessive production of ROS may lead to, for example, inflammatory tissue injury, carcinogenesis, atherosclerosis, and rheumatoid arthritis.[5] Genetic defects in membrane or cytosolic subunits of the NADPH oxidase enzyme (mostly in cyt b_{558}) result in chronic granulomatous disease (CGD), which is characterized by a high susceptibility of affected patients to bacterial and fungal infections.[6]

In recent years, it has become clear that gp91^{phox} has a number of homologues in a large variety of nonphagocytic cells.[7] Although the capacity of most members of this so-called Nox family to generate superoxide is modest, the ROS that they produce may have important functions in cell signaling and host defense.[8] Little is known about the regulation of these nonphagocyte Nox isoforms.[9]

* To whom correspondence should be addressed. Phone: +31 53 4894612. Fax: +31 53 4891105. E-mail: h.w.j.vanmanen@tnw.utwente.nl.
† University of Twente.
‡ University of Amsterdam.

Resonance Raman Imaging on Single Granulocytes

J. Phys. Chem. B, Vol. 108, No. 48, 2004 **18763**

Because heme-containing proteins such as cytochromes usually have several absorption bands in the visible region of the electromagnetic spectrum, they have been investigated extensively by resonance Raman (RR) spectroscopy.[10] In this technique, the inherently low Raman scattering from molecules of interest is dramatically enhanced by using an excitation wavelength at which these molecules show absorption. As a result, the RR spectrum shows bands that are highly selective for the chromophore under study. The investigation of cyt b_{558} from leukocytes has also benefited from RR investigations. An early report demonstrated that the heme in cyt b_{558} is low-spin, six-coordinate in both ferric and ferrous oxidation states.[11] Moreover, the authors, and others,[12] suggested imidazole or imidazolate axial ligation for the iron center of the heme. This was recently confirmed by identification of the four histidine residues, located in two transmembrane helices of gp91^{phox}, that are involved in axial ligation to the hemes.[13] We have previously investigated the activation of NADPH oxidase by both soluble and particulate activators by recording RR spectra from the cytoplasm of living neutrophils on a confocal Raman microspectrometer.[14,15] Upon activation, cyt b_{558} and MPO were partly reduced in these cells, whereas activated cyt b_{558}-deficient neutrophils from CGD patients did not show any MPO reduction at all, which is in line with earlier studies using absorption spectroscopy.[16] According to current consensus, (transient) reduction of cyt b_{558} can be taken as a sign for NADPH oxidase activity.[17]

To visualize the subcellular distribution of cyt b_{558} in leukocytes, and changes in this distribution upon cellular activation, immunocytochemistry in combination with fluorescence[18] and electron[19] microscopy has been commonly applied. However, cellular imaging techniques based on vibrational spectroscopy, such as infrared,[20] (resonance) Raman,[21] and coherent anti-Stokes Raman spectroscopy (CARS),[22] have several advantages over these methods. Most importantly, vibrational spectra provide detailed information about the chemical composition of the intracellular volume that is being probed. This is due to the narrow spectral bandwidth of vibrational bands compared to fluorescence bands. Details of molecular structure are thus provided that are unavailable from other microscopic modalities. Moreover, no sample labeling is required because the imaging contrast is produced by endogenous molecules. This minimizes sample disturbance and avoids artifacts due to labeling procedures. As a disadvantage, imaging time in vibrational microscopy may be long (minutes to hours) due to the long signal collection times necessary to generate high signal-to-noise ratios. This holds especially for infrared and Raman microscopy and in principle prohibits the study of fast dynamic intracellular processes. Through use of CARS microscopy, however, lipid droplet imaging in live fibroblast cells was recently reported with fast imaging times on the order of 1 s per frame.[23]

We recently demonstrated the feasibility of imaging the cyt b_{558} distribution in single neutrophils by resonance Raman microscopy.[24] Upon phagocytosis of small beads, a significant amount of the cyt b_{558} pool was found to be redistributed to the phagosome. Here, we present a detailed account of our RR imaging study on neutrophils and eosinophils. First, we discuss aspects such as the confocal parameters of our setup, the use of singular value decomposition as a spectral noise-reduction tool, and the effect of photobleaching on the Raman images. Next, a comparison is made between the cyt b_{558} distribution in neutrophils activated by phagocytosis and cells that were stimulated by phorbol 12-myristate 13-acetate (PMA). We show

that the amount of reduced cyt b_{558} in neutrophils activated with PMA is significantly higher than that in resting cells, confirming the notion that the reduction of cyt b_{558} signifies its activation. Finally, we demonstrate the versatility of our technique by showing RR imaging of the intracellular eosinophil peroxidase (EPO) distribution in a single eosinophil. This enzyme is involved in the killing of parasites by producing microbicidal hypohalites. Resonance Raman microscopy of heme-containing enzymes in cells of the innate immune system may become a favorable alternative to the microscopic techniques commonly applied in phagocyte biology. In particular, this type of vibrational spectroscopy provides a noninvasive, direct probe of enzymatic NADPH oxidase activity in leukocytes. It might also contribute to a better understanding of the expression, function, and activity of related Nox enzymes in a large range of other cell types and tissues.

Materials and Methods

Granulocyte Isolation and Adherence to CaF₂. Peripheral blood from healthy donors was obtained by venipuncture and collected in heparinized tubes. Granulocytes were isolated as previously described[25] and kept in PBS containing 0.5% BSA and 0.38% trisodium citrate (PBS-AC). CaF₂ slides (catalog no. 920-3516, Spectroscopy Central Ltd., Warrington, U.K.) were incubated overnight with 0.01% poly-L-lysine (PLL; catalog no. P1274, Sigma-Aldrich Chemie BV, Zwijndrecht, The Netherlands) at 4 °C and subsequently washed twice with PBS-AC. A few drops of the granulocyte suspension (typically 2×10^6 cells/mL) were added onto the PLL-coated CaF₂ substrate and incubated for 20 min at 37 °C. Unbound cells were removed by washing with PBS-AC.

Phagocytosis Experiments. Phagocytosis experiments with granulocytes were carried out with polystyrene beads (1.0 μm diameter; catalog no. 07310, Polysciences, Warrington, PA) that were opsonized by incubating the beads with fresh human serum for 1.5 h at 37 °C, followed by centrifugation and washing with PBS-AC ($2\times$). Typical concentrations of stock suspensions of opsonized beads were 10^9 particles/mL. Phagocytosis was initiated by adding 100 μL of a stock suspension of opsonized beads to granulocytes that had been adhered to a PLL-coated CaF₂ slide and incubated in 2 mL of phagocytosis buffer (PBS with 1 mM CaCl₂, 0.5 mM MgCl₂, 5 mM glucose, and 0.2% BSA). This mixture was incubated for 20 min at 37 °C and 5% CO₂, followed by washing with PBS ($2\times$) and fixing the cells in 2% paraformaldehyde in PBS for 20 min at room temperature. After being washed three times with PBS, the CaF₂ slide was transferred to a Petri dish (diameter 35 mm) and 2.5 mL of PBS was added. In some experiments, a few grains of sodium dithionite were subsequently added to reduce the heme groups of cytochrome b_{558}.

Stimulation of Granulocytes with PMA. Granulocytes adhering to a PLL-coated CaF₂ slide were incubated with 50 nM phorbol 12-myristate 13-acetate (PMA; catalog no. P8139, Sigma-Aldrich Chemie BV, Zwijndrecht, The Netherlands) in phagocytosis buffer for 20 min at 37 °C and 5% CO₂, after which the cells were washed with PBS and fixed in 2% paraformaldehyde in PBS for 20 min at room temperature. After being washed three times with PBS, the CaF₂ slide was transferred to a Petri dish (diameter 35 mm) and 2.5 mL of PBS was added.

Confocal Raman Microspectroscopy. All of the Raman measurements were performed on a previously described[26] home-built confocal Raman microscope that was adapted for resonant Raman imaging. Briefly, the 413.1 nm excitation

wavelength of a Kr-ion laser (Innova 90-K; Coherent, Santa Clara, CA) is reflected by a beam splitter (reflection 30%, transmission 70% at 413.1 nm) and focused by a $63\times/1.2$ NA water-immersion objective (Plan Neofluar; Carl Zeiss, Jena, Germany) onto the sample. The scattered light is collected by the same objective, transmitted through the beam splitter, filtered by a holographic notch filter (Kaiser Optical Systems, Ann Arbor, MI) to suppress reflected laser light and Rayleigh-scattered light, and focused onto a pinhole (25 μm diameter) at the entrance of an imaging spectrograph/monochromator (HR460; Jobin-Yvon, Paris, France) containing a blazed holographic grating with 1200 grooves/mm. A liquid-nitrogen-cooled CCD detector containing a back-illuminated chip with 1100×300 pixels of 24×24 μm^2 (LN/CCD 1100 PB/Visar; Princeton Instruments, Trenton, NJ) is placed in the focal plane of the spectrograph exit port, providing a spectral resolution of the Raman signal on the CCD camera of 2.1 cm^{-1}/pixel.

Resonance Raman Imaging. By use of a scanning mirror (Leica Lasertechnique GmbH, Heidelberg, Germany), data sets for Raman image construction were collected by scanning the laser beam across the cell of interest and recording a full RR spectrum (width approximately 2000 cm^{-1}) at each position. A step size of $\sim$0.5 μm was employed in the raster scanning of cells, which is larger than the lateral resolution of 0.33 μm (full width at half-maximum) of our setup.[24] Excitation powers and accumulation times per image pixel are given in the legends of the figures that display RR images. All of the spectra were corrected for the offset of the CCD camera and the frequency-dependent throughput of the setup. Further data analysis consisted of singular value decomposition of the spectral matrix, which acts as a noise-suppressing filter for the Raman spectra (see Results and Discussion). Finally, Raman images of a single cell were reconstructed by integrating the vibrational band of interest and subtraction of the background signal, which is most likely due to autofluorescence. All of the data manipulations were performed using routines written in MATLAB 6.5 (The MathWorks, Inc., Natick, MA).

Results and Discussion

Confocal Parameters of the Raman Microscope. Raman imaging on individual granulocytes (neutrophils and eosinophils) was performed on a previously reported[26] home-built confocal Raman microscope that was adapted for resonance Raman experiments (see Materials and Methods). To estimate the confocal parameters of our setup under these conditions, we employed a Gaussian beam approximation, which has been shown to correspond well with experimental data.[27] According to this approximation, the integral Raman intensity that passes through the pinhole from a planar object at a distance z from the focal plane scales as

$$I_{\text{ph}}(z) \propto 1 - \exp\left(\frac{-2R_{\text{ph}}^2}{\omega_{\text{ph}}^2}\right) \qquad (1)$$

where R_{ph} is the radius of the pinhole and ω_{ph} is the Gaussian beam waist at the position of the pinhole. The derivation of eq 1 has been published.[27] Figure 1 displays the normalized Raman intensity throughput as a function of axial displacement z for a number of pinholes. By use of a pinhole of 25 μm diameter in our measurements, the axial resolution (defined as the full width at half-maximum of the curves shown in Figure 1) is calculated to be 2.8 μm. The axial distance at which the intensity has fallen to $1/e^2$ of its peak value is 3.18 μm. The lateral resolution, defined as the $1/e^2$ diameter of the laser beam waist under the
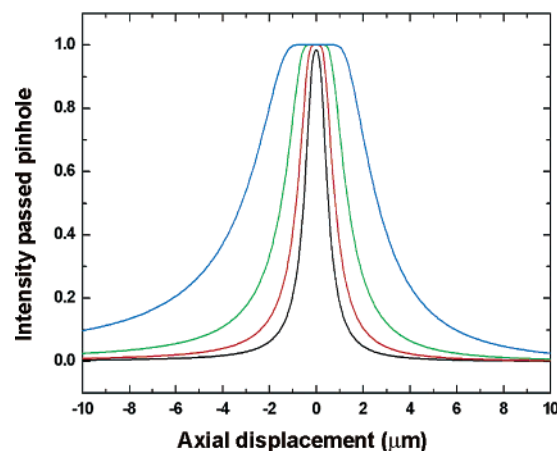
Figure 1. Calculated profiles of the Raman intensity that passes through confocal pinholes of varying diameters. Curves in blue, green, red, and black correspond to pinhole diameters of 50, 25, 15, and 10 μm, respectively, with respective full widths at half-maximum of 5.8, 2.8, 1.7, and 1.0 μm. For the calculations, the laser excitation wavelength was set to 413.1 nm, and the Raman scattering wavelength to 438.0 nm (corresponding to the 1375 cm^{-1} band of cytochrome b$_{558}$).

objective, is 0.32 μm according to the Gaussian beam approximation.

By use of lateral (r_0) and axial (z_0) $1/e^2$ radii of 0.16 and 3.18 μm, respectively, the effective focal volume ($V_{\text{eff}} = \pi^{3/2}r_0^2z_0$ for a three-dimensional (3D) Gaussian profile) of the confocal Raman microscope is 0.45 fL.

Singular Value Decomposition as Spectral Noise-Filtering Tool.[28] For Raman imaging experiments on single cells, we first position the focused laser excitation beam in a cell of interest (using a pellicle beam splitter, white-light illumination, and a videocamera). Subsequently, the beam is raster-scanned over the sample, and a full resonance Raman spectrum is collected at each position. A raw 3D data matrix (spatial $\times$ spatial $\times$ spectral) is thus acquired for each cell. We employ singular value decomposition (SVD)[29] on these matrixes (after converting them into 2D spatial $\times$ spectral matrixes) in order to significantly reduce the noise in the recorded RR spectra. In this method, the raw data matrix $\mathbf{A}$ is represented by two sets of vectors that are weighted by their corresponding singular values. In mathematical terms, the $N \times M$ matrix $\mathbf{A}$ is decomposed into three matrixes $\mathbf{U}$, $\mathbf{S}$, and $\mathbf{V}$ according to

$$\mathbf{A} = \mathbf{U} \cdot \mathbf{S} \cdot \mathbf{V}^{\mathbf{T}} \qquad (2)$$

where $\mathbf{U}$ is an $N \times N$ matrix containing the left set of singular vectors (lSV), $\mathbf{V}$ is an $M \times M$ matrix containing the right set of singular vectors (rSV), and $\mathbf{S}$ is an $N \times M$ diagonal matrix where the diagonal elements represent, in decreasing order, the singular values. Under our data recording conditions, where RR spectra are obtained as a function of position in the cell, the lSV is a position-independent orthonormal basis set from which all position-dependent RR spectra are constructed, whereas the vectors from the rSV take into account the position-dependent variation of the corresponding vectors in the lSV. Singular values correspond to the degree that their respective lSV and rSV vectors contribute to the data matrix. By use of only the first $n < N$ significant values of $\mathbf{S}$ (this results in $\mathbf{S}_{\text{rec}}$), the noise-filtered data matrix $\mathbf{A}_{\text{rec}}$ is reconstructed using

$$\mathbf{A}_{\text{rec}} = \mathbf{U} \cdot \mathbf{S}_{\text{rec}} \cdot \mathbf{V}^{\mathbf{T}} \qquad (3)$$

In the application of SVD, the user input thus consists of
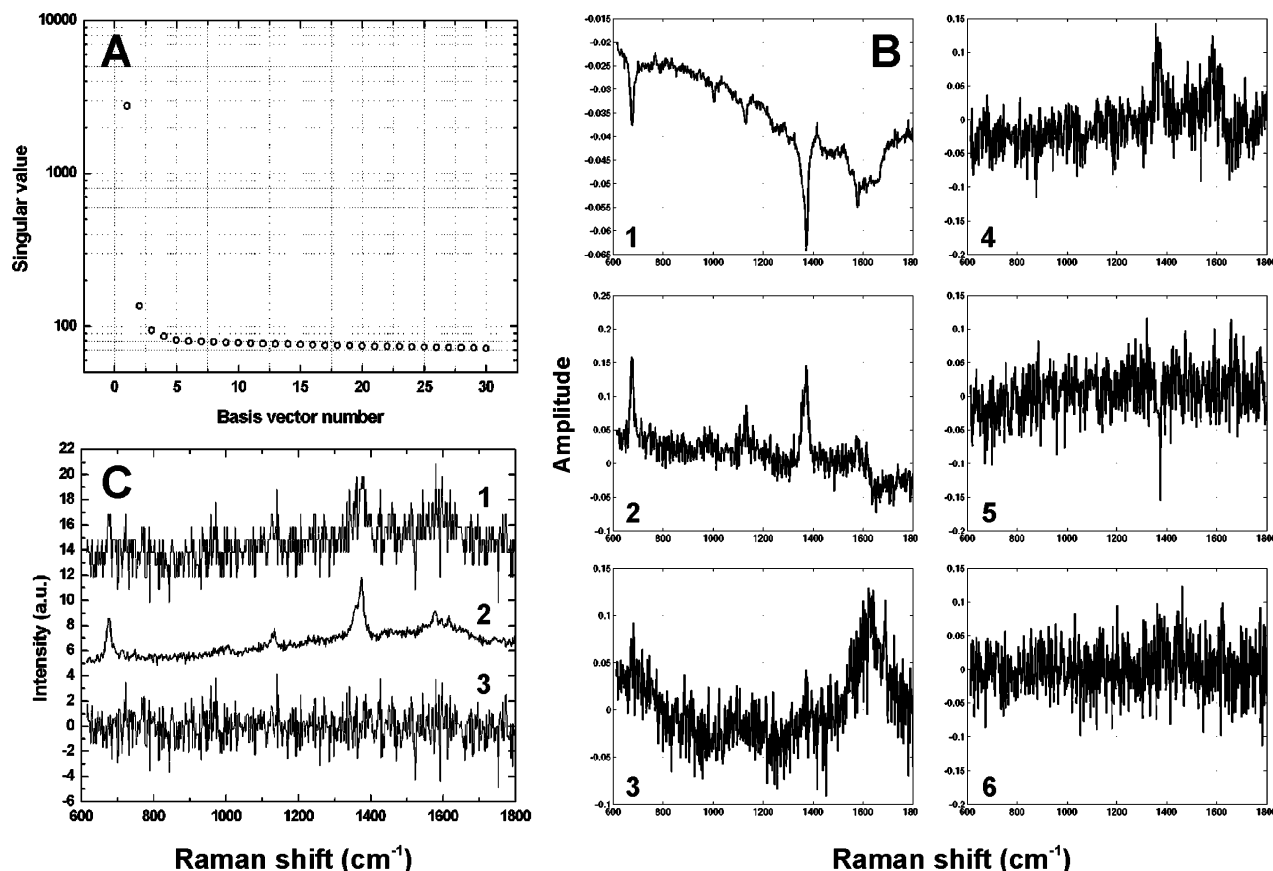
Figure 2. Results of singular value decomposition (SVD) analysis on the 3D-spectral matrix obtained during Raman imaging of cytochrome b_{558} in a single, resting neutrophil. (A) Semilogarithmic plot of the first 30 singular values. (B) Plots of the first six basis vectors resulting from SVD. For spectral matrix reconstruction, only the first five basis vectors were employed. (C) Results of spectral filtering using SVD. Spectrum 1 is a RR spectrum from the cytoplasm of a resting neutrophil, acquired during imaging of cytochrome b_{558} in a single cell. Spectrum 2 is the same spectrum, reconstructed after SVD on the whole spectral matrix and rejection of noise-containing basis vectors. Spectrum 3 is the difference spectrum (1 minus 2) with a mean intensity of 0.001. Spectra 1 and 2 have been shifted along the ordinate for clarity.

estimating the number of significant singular values. This number is determined according to criteria reported by others.[30] Figure 2 displays the results of SVD on a data matrix obtained from RR imaging on a single, resting neutrophil.

Inspection of Figure 2A reveals that the first four to five singular values deviate from the slowly declining background. This is consistent with Figure 2B, which shows that only the first five basis vectors contain relevant spectral information above the noise level. It should be kept in mind that these basis vectors do not correspond directly to true spectra of the investigated sample, but rather are mathematical constructs from which true spectra may be reconstructed. This explains the appearance of both positive and negative features in the vectors shown in Figure 2B. From the sixth basis vector (Figure 2B6), the autocorrelation functions of the basis vectors are approximated by delta functions (not shown) and thus contain predominantly noise. For this particular example, five relevant singular values were employed in the reconstruction of the data matrix. The difference between raw and SVD-reconstructed RR spectra is exemplified by Figure 2C. Significant improvement in the signal-to-noise ratio of the RR spectrum is observed, signifying that SVD can be used as a powerful noise-filtering tool in the treatment of large spectroscopic data sets. We apply it routinely to all of our recorded Raman imaging data.

Photobleaching of the Raman Signal. Spontaneous Raman spectroscopy on single cells is hampered by low signal intensities due to the very small Raman scattering cross sections of the biological macromolecules involved. This necessitates the use of laser excitation powers in the 1−100 mW range in

order to avoid very long signal collection times. In previous work, we have thoroughly investigated the effect of high laser powers on both the reproducibility of Raman spectra recorded from living and fixed cells and the viability of the cells after the measurements.[21a,31] For example, it was found that sample degradation occurs with 514.5 nm excitation light but not with 660 nm.[31] It was suggested that photochemical reactions were most likely responsible for the degradation processes. In a recent study on fixed cells from our group, it was shown that nonresonant Raman imaging can be performed at 100 mW 647 nm excitation in combination with an accumulation time of 1 s/pixel without loss of Raman signal.[21a] As in fluorescence, excitation under conditions where resonance Raman scattering occurs results in the population of electronically excited states by the molecules that absorb at the excitation wavelength used. It is therefore expected that photobleaching of the Raman signal is much more prominent in resonant than in nonresonant Raman spectroscopy, even though much lower laser powers are employed in resonant Raman experiments. We investigated the photobleaching of the cytochrome b_{558} Raman signal in fixed neutrophils by recording 10 consecutive spectra from the same spot in the cytoplasm of single cells. Figure 3 demonstrates that, for all three different situations used (see caption), the decrease in the integrated intensity of the strong 1375 cm^{-1} band of cyt b_{558} can be fitted well with first-order exponential decay curves (i.e., $y = A \exp(-k_{bl}x) + c$, where y is the Raman intensity, A is the intensity at the ordinate (at $x = 0$), x is the total supplied excitation dose, k_{bl} is the photobleaching rate constant, and c is a constant background).
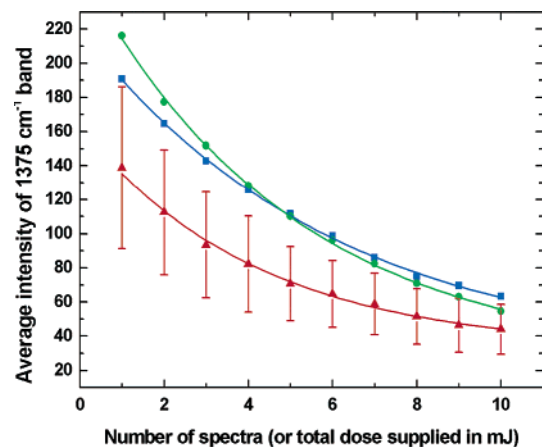
Figure 3. Photobleaching of the cytochrome b_{558} RR signal at 413.1 nm excitation. For the construction of each curve, 10 consecutive Raman spectra were taken at one position in the cytoplasm of an unstimulated neutrophil, and this procedure was performed for 20 randomly selected cells. The total intensity of the 1375 cm^{-1} band, averaged over 20 cells, is plotted as a function of spectrum number (or total supplied excitation dose). The three curves represent three different excitation conditions; however, the supplied dose was identical in each situation (1 mJ per point). The applied excitation power and the accumulation time per spectrum were as follows: blue, 0.5 mW and 2.0 s; green, 1.0 mW and 1.0 s; red, 2.0 mW and 0.5 s. Error bars showing the standard deviations are given for the lower curve only. They are similar for the other two curves, and they mainly originate from cell-to-cell variations in the RR signal of cyt b_{558}.

Analysis of the three curves in Figure 3 revealed that the mean intensities of the lowest curve (2 mW, 0.5 s/spectrum) are significantly different from the mean intensities of the upper curves (at the 99% confidence level), whereas the mean intensities of the upper two curves are not significantly different (independent two-sample t-test with unequal variances). The lowest curve also has the largest photobleaching rate constant (0.26 ± 0.02 versus 0.17 ± 0.01 (0.5 mW, 2 s) and 0.20 ± 0.01 (1 mW, 1 s)). At present, we have no clear explanation for the lower absolute Raman signal intensities at 2 mW, 0.5 s/spectrum compared to the other two cases. On the basis of these results, however, we avoided the use of 2 mW excitation power in subsequent Raman imaging studies. Instead, we chose the fastest of the two alternatives, namely, 1 mW and 1 s/pixel in Raman imaging experiments on neutrophils.

The fact that the photobleaching of the RR signal from cyt b_{558} can be described by a first-order exponential decay means that the relative amount of bleaching is independent of the cyt b_{558} concentration in the cell. As a consequence, there is no distortion in the Raman images shown here because the effect of photobleaching on the intensity of the cyt b_{558} signal is relatively the same everywhere in the cell.

Resonance Raman Detection Limit of Cytochrome b_{558} in Neutrophils. As mentioned before, Raman spectroscopy suffers from low signal intensities due to the low Raman scattering cross sections of most biologically relevant molecules. However, by use of high excitation powers (10−100 mW) and long accumulation times (seconds to minutes), nonresonant Raman spectroscopy on cells results in high-quality signals from ubiquitous cellular compounds such as DNA, RNA, proteins, and lipids.[21a,32] It becomes feasible to detect specific molecules if their concentration in the cell is high and their Raman signal can be enhanced by resonance. This is the case for cyt b_{558} in neutrophils and EPO in eosinophils. To estimate the RR detection limit of cyt b_{558} in a single neutrophil, we first calculated the average number of cyt b_{558} molecules per granule
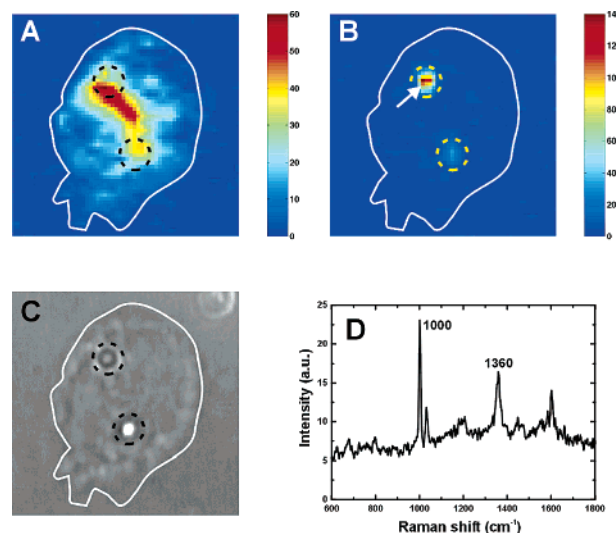
Figure 4. Resonant Raman images ($15 \times 15 \ \mu m^2$) of a neutrophil with two phagocytosed PS beads. (A) RR image constructed in the 1360 cm^{-1} band of cyt b_{558}. (B) Nonresonant Raman image constructed in the 1000 cm^{-1} band of PS. (C) Corresponding white-light transmission image. The position of the PS beads in A, B, and C is indicated with circles, whereas the outline of the cell is marked white. (D) Raman spectrum from the position indicated by the white arrow in B. Conditions for images A and B: λ_{exc} = 413.1 nm (1 mW), 1 s accumulation time/pixel.

to be ∼5000 based on the following data: (1) the average amount of cyt b_{558} per neutrophil is 10^{-17} mol;[33] (2) specific granules and secretory vesicles contain 80−90% of the total cyt b_{558} pool in resting cells;[34] (3) mature neutrophils contain approximately 1000 specific granules (diameter 0.2−0.5 μm) per cell.[35] Because the lateral size of the excitation volume ($1/e^2$ diameter of 0.32 μm) is approximately the same as the diameter of a specific granule, the RR signal from cyt b_{558} in a neutrophil will be maximized when multiple granules are positioned in a row along the optical axis (i.e., stacked on top of each other). This is not very likely to occur inside a cell, however, and we estimate that a maximum of five granules (corresponding to ∼25 000 molecules) is probed at one instant. RR spectra (not shown) from concentrated cyt b_{558} regions (e.g., the red region shown in Figure 4A) indicate that the detection limit for cyt b_{558} is ∼10% of these high-intensity regions. Thus, under typical RR imaging conditions, we can detect approximately 2500 cyt b_{558} molecules intracellularly.

Contribution of Myeloperoxidase to the RR Signal from Neutrophils. The Raman signal originating from cyt b_{558} in neutrophils is enhanced by resonance at 413.1 nm excitation because native (oxidized) cyt b_{558} displays a very strong Soret absorption band centered at this wavelength. Besides cyt b_{558}, neutrophils contain large amounts of the hemoprotein myeloperoxidase (MPO) concentrated in azurophilic granules. Whereas other mammalian peroxidases such as lactoperoxidase (LPO) and eosinophil peroxidase (EPO) also have Soret bands around 413 nm, the visible absorption band of MPO is red-shifted to 428 nm.[36] This is caused by a covalent sulfonium ion linkage between a vinyl group of the heme prosthetic group and the Met[243] amino acid residue in close proximity to it, as revealed by mutation studies.[37] Due to this red-shifted absorption, a weaker enhancement of the RR signal from MPO compared to that from cyt b_{558} is thus expected upon 413.1 nm excitation. However, the contribution of MPO to the RR signal from neutrophils is not negligible, and previous studies in our group indicated that neutrophilic RR spectra can best be described by a linear combination of RR spectra from azurophilic (containing

Resonance Raman Imaging on Single Granulocytes

J. Phys. Chem. B, Vol. 108, No. 48, 2004 **18767**

MPO) and specific (containing cyt b_{558}) granules.[26] Diagnostic features to distinguish MPO from cyt b_{558} on the basis of RR spectra include the relative intensity of the ν_7 porphyrin mode at 678 cm^{-1}, the presence of porphyrin modes at 1116 (MPO) or 1130 cm^{-1} (cyt b_{558}), and the position and intensity of porphyrin and vinyl modes in the 1420−1640 cm^{-1} region.[26] By application of these criteria to RR imaging data sets recorded from neutrophils, it becomes apparent that the major contribution to the RR signal from these cells at 413.1 nm excitation comes from cyt b_{558}. The discussion of RR imaging results on neutrophils presented here is therefore focused on cyt b_{558}, although it must be kept in mind that MPO may contribute to some extent to the RR signal from these leukocytes.

Resonance Raman Imaging on Single Neutrophils. We recently reported the feasibility of imaging the intracellular cyt b_{558} distribution in single neutrophils by resonance Raman microscopy.[24] We showed that in cells that had phagocytosed polystyrene (PS) beads part of the cytochrome b_{558} pool translocated to the bead-containing phagosome. The neutrophil shown in Figure 4 clearly exhibits this behavior as well. In this case, the iron centers of the heme groups in cyt b_{558} were first reduced with sodium dithionite. We found that after chemical reduction with this agent the cyt b_{558} was less prone to photobleaching. Sodium dithionite is a known antioxidant and is used to prepare anoxic solutions.[38] It is therefore likely that oxygen is involved in the photobleaching of cyt b_{558}.[39] The RR image shown in Figure 4A was thus constructed in the reduced 1360 cm^{-1} band of cyt b_{558}. Large amounts of cytochrome b_{558} are found near the upper ingested bead. Because the polystyrene beads give rise to high nonresonant Raman signal intensities, the same recorded data set can also be used to construct Raman images of these beads (Figure 4B). From the white-light transmission image (Figure 4C), it is seen that two beads have been ingested by the neutrophil. They do not reside in the same focal plane, and this causes the large difference in signal intensities observed in Figure 4B.

Figure 4D shows the Raman spectrum from the position indicated by the arrow in Figure 4B. The presence of strong Raman signals from both polystyrene (band at 1000 cm^{-1}) and cytochrome b_{558} (band at 1360 cm^{-1}) arising from the sub-femtoliter focal volume confirms the close association of cytochrome b_{558} with the phagosome. Secondary granules and secretory vesicles, which contain 80−90% of the total cytochrome b_{558} pool in resting cells, translocate to and fuse with the developing phagosome upon particle ingestion.[40] After additional binding of several activating and regulatory proteins translocating from the cytosol to phagosomal cytochrome b_{558},[1a] superoxide is released into the phagosome by the activated NADPH oxidase.

Besides phagocytosis, the activation of granulocytes can also be triggered by chemical agonists such as PMA and the Ca^{2+} ionophore A23187, by biologically active lipids such as arachidonic acid and phosphatidic acid, and by chemotaxins such as fMLP.[41] As a direct activator of protein kinase C, which is an important intracellular signaling enzyme,[42] PMA is one of the most potent neutrophil stimulants known. Using confocal Raman microspectroscopy, we demonstrated that treatment of neutrophils with PMA resulted in a partial reduction of the intracellular cytochrome b_{558} heme groups, as reflected by a shift in the heme iron oxidation state marker band from 1375 to 1360 cm^{-1}.[15] This confirms that the heme groups of cytochrome b_{558} take part in the electron transport chain from NADPH to O$_2$ in the activated NADPH oxidase enzyme. Because they are embedded in the membrane, the hemes bridge the large distance from the

FAD cofactor that is bound on the cytosolic side of cytochrome b_{558} to the oxygen that is present extracellularly.

It has been reported that upon PMA treatment of neutrophils a large fraction of the intracellular cytochrome b_{558} pool translocates to the plasma membrane, where fusion of the membranes from secondary granules and secretory vesicles with the plasma membrane occurs.[34] We performed resonance Raman imaging experiments to visualize the cyt b_{558} distribution in single neutrophils that had been subjected to PMA stimulation. The RR image shown in Figure 5A reveals that most of the cyt b_{558} is present near the cell periphery, which is in line with the translocation process described above. In contrast, phagocytosis of beads by neutrophils leads to cyt b_{558} translocation to the beads and not to the plasma membrane, as demonstrated by the RR image in Figure 4A.

The sample used for RR imaging of PMA-stimulated cells was not reduced with sodium dithionite, because it was anticipated that part of the cyt b_{558} (and MPO) pool is reduced upon PMA treatment.[15,43] This leads to separated Raman signals for oxidized and reduced cyt b_{558} in the cell, and we expected that it might be possible to image the subcellular localization of these two states in a single cell. The RR spectrum displayed in Figure 5D is the average spectrum from the regions in Figure 5A containing large amounts of cyt b_{558}. The shoulder at 1363 cm^{-1} is assigned to reduced cyt b_{558}. We found that in the RR image displayed in Figure 5A the pixel-to-pixel variation in the intensity ratio of reduced to oxidized cyt b_{558} is rather small. In other words, most spectra from individual pixels resemble the average spectrum shown in Figure 5D with reduced/oxidized ratios[44] ranging from 0.41 to 0.86 and an average ratio of 0.68 ± 0.10.[45] A similar analysis on an unstimulated, adhered neutrophil (RR image not shown) yielded an average reduced/oxidized cyt b_{558} ratio of 0.39 ± 0.05. In addition, RR spectra recorded from the cytoplasm of freshly adhered, live neutrophils (5 s signal accumulation time per cell at 1 mW excitation power) also showed minor contributions from reduced cyt b_{558}. This indicates that the appearance of the 1363 cm^{-1} band, and thus the reduction of cyt b_{558}, is not induced by the fixation procedure. The fact that there is a significant amount of reduced cyt b_{558} in unstimulated cells is rather surprising, and it suggests that the granulocyte isolation procedure or the adsorption of the cells onto the substrate may lead to some activation (and thus reduction) of cyt b_{558}. In accordance with this, Demaurex et al. reported that spreading of neutrophils on a substrate is associated with superoxide production.[46] In any case, our analysis shows that upon PMA stimulation there is a significant increase in the amount of reduced intracellular cyt b_{558} present in the cell, reflecting NADPH oxidase activity. The small intracellular variations in the reduced/oxidized cyt b_{558} ratio may be explained by the fact that PMA acts on the cell in an unpolarized manner because a constant, homogeneous dose is applied to the sample. Moreover, the intracellular volume that is probed by the confocal Raman microscope is still large with respect to the size of granules/vesicles and the molecules of cyt b_{558} that are contained in them. This inherently results in averaging of the Raman signal from the many heme moieties that will be probed by the laser focus at any instant. Some of these issues are being addressed in our laboratory. For example, phagocytosis experiments with neutrophils might lead to more localized activation of cyt b_{558} than PMA stimulation, because phagocytosis is a highly polarized cellular event. Moreover, activation of cells under anaerobic conditions may result in a higher amount of reduced cyt b_{558},[43] which will facilitate quantification studies.
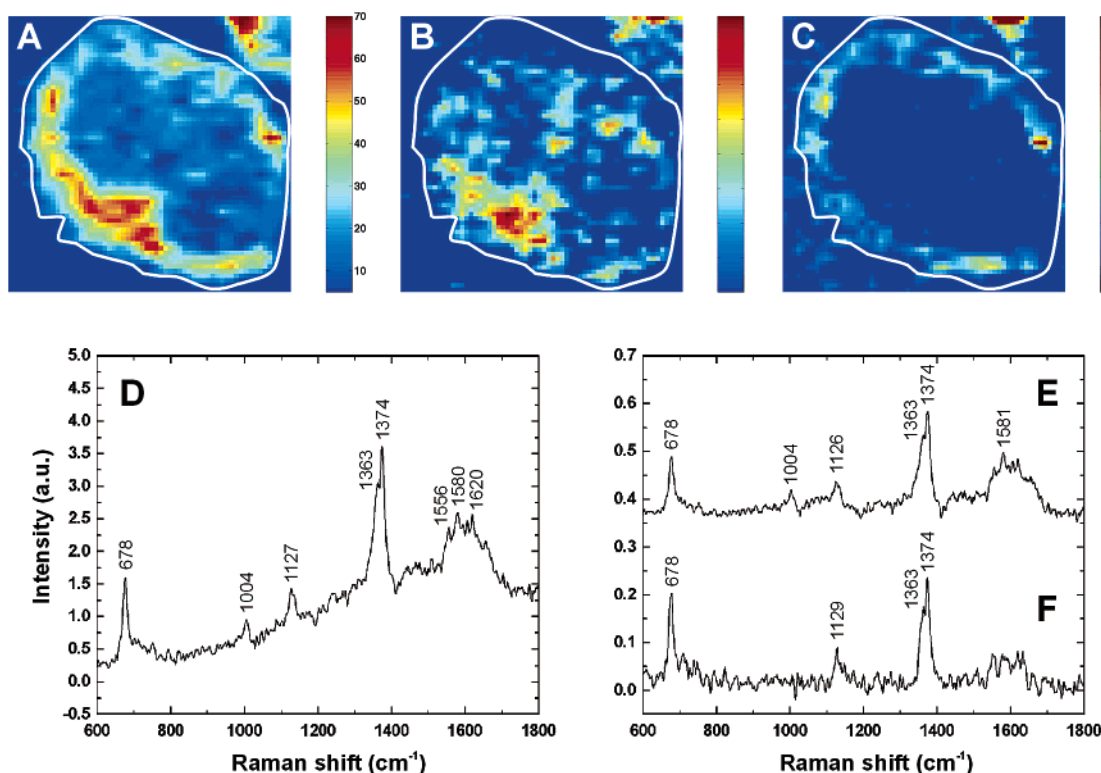
Figure 5. Images (15 × 15 μm²) and RR spectra of a neutrophil activated with PMA for 20 min. The outline of the cell is marked white. (A) RR image constructed in the combined 1363/1374 cm⁻¹ bands of cyt b$_{558}$. (B) SVD coefficient image corresponding to basis vector 1. (C) SVD coefficient image corresponding to basis vector 3. (D) Average RR spectrum from the high-intensity regions (plotted in yellow/red) of the cell shown in A. (E) First basis vector resulting from SVD analysis. (F) Third basis vector resulting from SVD analysis. Background signal in E and F (but not in D) was subtracted. Conditions for RR imaging: λ_{exc} = 413.1 nm (1 mW), 1 s accumulation time/pixel.

As discussed above, MPO contributes to some extent to the RR signal obtained from neutrophils. Because there are detectable differences between the RR signal of MPO and cyt b$_{558}$, we anticipated that the application of data analysis methods to recorded RR imaging data sets might reveal differences between the subcellular distribution of MPO and cyt b$_{558}$. Singular value decomposition on the data set used to construct the RR image displayed in Figure 5A resulted in the different basis vectors plotted in parts E and F of Figure 5. Whereas the first basis vector shown in Figure 5E resembles the average spectrum displayed in Figure 5D, the third basis vector (plotted in Figure 5F) differs significantly from these spectra.[47] The relative intensity of the 678 cm⁻¹ band and the appearance and intensities of the bands in the 1420−1640 cm⁻¹ region suggest that the basis vector shown in Figure 5F describes relatively pure cyt b$_{558}$, whereas the first basis vector (Figure 5E) and the average RR spectrum (Figure 5D) describe cyt b$_{558}$ mixed with some MPO.[26] The relative contribution of these basis vectors to the total RR signal in each position of the image can be assessed by constructing a coefficient matrix $\mathbf{C}$ ($\mathbf{C} = \mathbf{S}_{rec} \cdot \mathbf{V}^T$, see also the section on SVD) and plotting the coefficients as a function of position. This results in panels B and C of Figure 5 for the first and third basis vector, respectively. Comparison of these images indicates that the relatively pure cyt b$_{558}$, probably from specific granules, can be found closer to the cell periphery than the mixed cyt b$_{558}$/MPO fraction. Stimulation of neutrophils with PMA leads to extensive degranulation (or exocytosis) of secretory vesicles and different kinds of granules. Interestingly, a hierarchical mobilization of these organelles has been reported, with specific granules being exocytosed more readily than azurophilic granules.[40b] This behavior is also suggested by the SVD coefficient images shown in panels B and C of Figure 5,
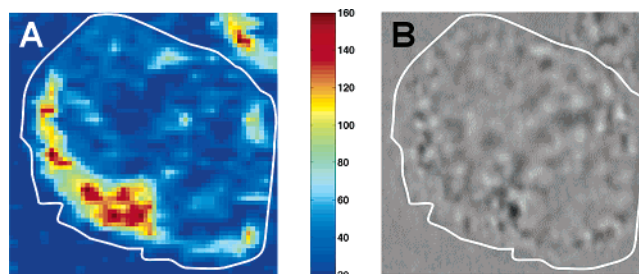

Figure 6. Rayleigh and white-light transmisson images (15 × 15 μm²) of the same cell as shown in Figure 5. (A) Rayleigh image constructed in the 0 cm⁻¹ band. (B) White-light transmission image. The outline of the cell is marked white.

and this again demonstrates the versatility of SVD as a powerful data analysis tool.

Our Raman imaging method involves recording a full RR spectrum at each position in the predefined region of interest. Under our conditions, this means that the Rayleigh scattering signal at 0 cm⁻¹ is also available for imaging. A Rayleigh image constructed from the same data set as the one used to construct the Raman image in Figure 5A is shown in Figure 6A.

At first glance, both images look similar. This is explained by the fact that most of the cyt b$_{558}$ is present in specific granules and secretory vesicles of 0.2−0.5 μm size, and it is expected that granules of this size are strong scatterers. Granular structures seen in the white-light transmission image shown in Figure 6B seem to colocalize with regions of high scattering intensity in Figure 6A, although these images cannot be compared directly because Figure 6A is a confocal image and Figure 6B is not. Differences between the Raman image and the Rayleigh image may be caused by other scattering organelles, such as the azurophilic granules. Mature neutrophils contain over 200

Resonance Raman Imaging on Single Granulocytes

J. Phys. Chem. B, Vol. 108, No. 48, 2004 **18769**
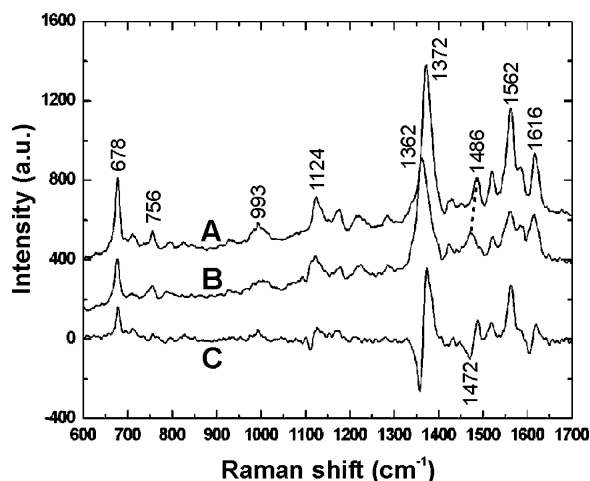
Figure 7. RR spectra from the cytoplasm of a (A) native and a (B) dithionite-reduced fixed eosinophil. Conditions: $\lambda_{exc} = 413.1$ nm (1 mW), 10 s accumulation time, $7.5 \times 7.5 \ \mu m^2$ area scanned during signal accumulation (1 s/scan). Spectrum C is the difference spectrum (A minus B). Spectrum A has been shifted along the ordinate for clarity.
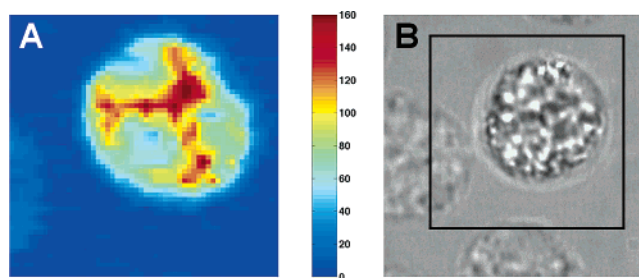

Figure 8. Raman image of the eosinophil peroxidase (EPO) distribution in a single eosinophil. (A) RR image ($15 \times 15 \ \mu m^2$) in the 1362 cm^{-1} band of a fixed eosinophil. Conditions: $\lambda_{exc} = 413.1$ nm (0.5 mW), 1 s accumulation time/pixel. Note the low Raman intensity from the neutrophil on the left side of the eosinophil. (B) Corresponding white-light transmission image. The area enclosed by the black square was used for RR imaging.

granules per ultrathin section,[35a] allowing high Rayleigh scattering intensities to be recorded from these cells. Thus, additional information can be gained from data sets recorded during Raman imaging by considering the Rayleigh scattering band.

Resonance Raman Imaging on Single Eosinophils. Neutrophils form the majority of the leukocyte fraction from peripheral blood. In contrast, eosinophils represent approximately 1−3% of the total amount of white blood cells. These are potent proinflammatory cells that, like neutrophils, are critical in host defense, particularly in parasitic infections, and are believed to play a pathogenic role in diseases such as allergic and immunological disorders and some neoplastic diseases.[48] In addition to a significant pool of cytochrome b_{558},[49] eosinophils contain large amounts of eosinophil peroxidase (EPO), which is concentrated in the matrix of the specific granules. Similar to MPO in neutrophils, EPO from eosinophils is responsible for the enzymatic conversion of hydrogen peroxide to cytocidal hypohalites used in the killing process of parasites or other infectious organisms. However, whereas hypochlorous acid is the main cytotoxic agent produced by MPO, bromide is the preferred substrate for EPO.[50]

Previous RR spectroscopic characterization of EPO inside live human eosinophils in our group demonstrated that the prosthetic group in the resting enzyme is a high-spin, six-coordinate, ferric protoporphyrin IX.[51] Even under 660 nm excitation, the Raman signal obtained from eosinophils is almost exclusively due to EPO because of a charge-transfer absorption band centered at ~640 nm, which leads to resonance enhancement of the EPO Raman signal. The same holds for 647 nm excitation, which we employ in our laboratory for nonresonant Raman imaging on a variety of cells.[21a]

We performed resonance Raman spectroscopy and microscopy on single eosinophils using 413.1 nm excitation in order to visualize the intracellular EPO distribution. Fast scanning over a single eosinophil for 10 s at 1 mW excitation power leads to high-quality RR spectra, as shown in Figure 7.

The oxidized-minus-reduced spectrum displayed in Figure 7C shows that, upon reduction of the heme iron center by dithionite, prominent shifts in the Raman bands at 1372 and 1486 cm^{-1} occur (to 1362 and 1472 cm^{-1}, respectively). These bands are assigned to the ν_4 and ν_3 porphyrin modes, respectively, which are both oxidation-state marker bands of the central iron.[51] In addition, the ν_3 mode is also a marker for the iron spin state.

Its shift from 1486 to 1472 cm^{-1} upon reduction suggests a high-spin coordination environment in both iron oxidation states.[52]

As mentioned above, eosinophils also contain cytochrome b_{558}. However, the RR signal from cyt b_{558} in eosinophils at 413.1 nm excitation cannot be distinguished in the spectra displayed in Figure 7 because it is overwhelmed by the EPO RR signal. Both cyt b_{558} and EPO have Soret absorption bands centered at 413 nm, which is due to the similarity of the prosthetic groups in these hemoproteins. The Raman signal from both species will be strongly enhanced by resonance at 413.1 nm excitation, and it cannot be excluded that the Raman spectra shown in Figure 7 contain signal contributions from cyt b_{558}. A selective EPO Raman signal from eosinophils can be obtained by performing experiments at 660[51] or 647[53] nm excitation.

Although present in low numbers, eosinophils could be easily selected for RR imaging in a granulocyte sample because they are readily distinguished from neutrophils by white-light transmission microscopy. This is clearly demonstrated in Figure 8B, and the corresponding RR image constructed in the 1362 cm^{-1} band of the resting, reduced eosinophil is shown in Figure 8A.

Because the Raman signal from intracellular EPO is much higher than the cyt b_{558} signal from neutrophils, the excitation power was 0.5 mW instead of 1 mW used for neutrophil RR imaging. The difference in signal intensity between eosinophils and neutrophils is exemplified by the low intensity in Figure 8A from the neutrophil on the left side of the eosinophil. The eosinophil in this image contains a heterogeneous intracellular distribution of EPO, confirming its presence in granules. The cytoplasm of eosinophils is packed with ~200 granules, of which there are four distinct populations.[48] Only the secondary granules contain EPO, so RR imaging is a convenient label-free tool to distinguish these granules from the other three types (primary granules, small granules, and lipid bodies). As evident from Figure 8A, the small size of the granules, in combination with the employed step size of 500 nm, precludes the observation of individual EPO-containing granules in this image. By a decrease in the imaged region and the step size during imaging, single granules might be successfully visualized. Care must be taken in pursuing this goal because EPO is prone to photobleaching at 413.1 nm excitation. Experiments at 647 nm excitation, however, have recently demonstrated the possibility of imaging individual EPO-containing granules in eosinophils.[53]

Conclusions

Confocal resonance Raman microscopy has been applied to map the intracellular distribution of heme-containing enzymes

18770 *J. Phys. Chem. B, Vol. 108, No. 48, 2004*

van Manen et al.

that are important in the innate immune response from granulocytes. The Raman signal from both cytochrome b_{558} in neutrophils and eosinophil peroxidase (EPO) in eosinophils is resonantly enhanced by exciting these hemoproteins in their Soret absorption band, using 413.1 nm as excitation wavelength. This enables the selective imaging of these enzymes in single cells. Several important aspects of the resonance Raman imaging process have been discussed here, namely, the estimation of the confocal parameters of the confocal Raman microscope, the use of singular value decomposition as a noise-filtering tool for the recorded spectral data, and the influence of photobleaching on the Raman signal intensities during imaging at 413.1 nm excitation. The contribution of myeloperoxidase (MPO) to the RR signal from neutrophils has also been addressed.

Resonance Raman imaging experiments on neutrophils revealed that, upon phagocytosis of latex beads, part of the intracellular cytochrome b_{558} pool is redistributed to the phagosome. The presence of both polystyrene and cytochrome b_{558} Raman signals in the subfemtoliter volume defined by the confocal microscope confirms the spatial proximity of these components in phagosomal regions. Stimulation of neutrophils with PMA resulted in partial reduction of the heme iron moieties, as reflected by a spectral shift in the most intense RR band of cytochrome b_{558}. The amount of heme reduction upon stimulation was largely uniform across the cell. Adhered neutrophils without PMA treatment displayed a significantly lower amount of heme reduction. Additional information was obtained from recorded data sets by constructing images in the 0 cm^{-1} band, which is due to Rayleigh scattering. Finally, RR imaging on eosinophils revealed the intracellular EPO distribution in single eosinophils.

We believe that the cellular imaging technique described here, based on resonance Raman spectroscopy, has the potential to become the method of choice for the intracellular study of heme-containing enzymes involved in innate immunity. The label-free nature of our method and the facile sample preparation are major advantages in this regard, as they avoid artifacts and cell disturbance.

References and Notes

(1) For recent overviews of NADPH oxidase, see: (a) Vignais, P. V. *Cell. Mol. Life Sci.* **2002**, *59*, 1428−1459. (b) Babior, B. M. *Blood* **1999**, *93*, 1464−1476.

(2) Reeves, E. P.; Lu, H.; Lortat Jacobs, H.; Messina, C. G. M.; Bolsover, S.; Gabella, G.; Potma, E. O.; Warley, A.; Roes, J.; Segal, A. W. *Nature* **2002**, *416*, 291−297.

(3) Winterbourn, C. C.; Vissers, M. C. M.; Kettle, A. J. *Curr. Opin. Hematol.* **2000**, *7*, 53−58.

(4) Leusen, J. H. W.; Verhoeven, A. J.; Roos, D. *J. Lab. Clin. Med.* **1996**, *128*, 461−476.

(5) Babior, B. M. *Am. J. Med.* **2000**, *109*, 33−44.

(6) Heyworth, P. G.; Cross, A. R.; Curnutte, J. T. *Curr. Opin. Immunol.* **2003**, *15*, 578−584.

(7) Lambeth, J. D. *Curr. Opin. Hematol.* **2002**, *9*, 11−17.

(8) Finkel, T. *Curr. Opin. Cell Biol.* **2003**, *15*, 247−254.

(9) Bokoch, G. M.; Knaus, U. G. *Trends Biochem. Sci.* **2003**, *28*, 502−508.

(10) For some overviews, see: (a) Spiro, T. G. *Resonance Raman Spectra of Heme and Metalloproteins*; Wiley: New York, 1987. (b) Tu, A. T. *Raman Spectroscopy in Biology: Principles and Applications*; John Wiley & Sons: New York, 1982; Chapter 12.

(11) Hurst, J. K.; Loehr, T. M.; Curnutte, J. T.; Rosen, H. *J. Biol. Chem.* **1991**, *266*, 1627−1634.

(12) (a) Ueno, I.; Fujii, S.; Ohya-Nishiguchi, H.; Iizuka, T.; Kanegasaki, S. *FEBS Lett.* **1991**, *281*, 130−132. (b) Fujii, H.; Finnegan, M. G.; Miki, T.; Crouse, B. R.; Kakinuma, K.; Johnson, M. K. *FEBS Lett.* **1995**, *377*, 345−348.

(13) Biberstine-Kinkade, K. J.; DeLeo, F. R.; Epstein, R. I.; LeRoy, B. A.; Nauseef, W. M.; Dinauer, M. C. *J. Biol. Chem.* **2001**, *276*, 31105−31112.

(14) Otto, C.; Sijtsema, N. M.; Greve, J. *Eur. Biophys. J.* **1998**, *27*, 582−589.

(15) Sijtsema, N. M.; Tibbe, A. G. J.; Segers-Nolten, G. M. J.; Verhoeven, A. J.; Weening, R. S.; Greve, J.; Otto, C. *Biophys. J.* **2000**, *78*, 2606−2613.

(16) Segal, A. W.; Jones, O. T. G. *FEBS Lett.* **1980**, *110*, 111−114.

(17) Babior, B. M. *Curr. Opin. Immunol.* **2004**, *16*, 42−47.

(18) (a) DeLeo, F. R.; Allen, L.-A. H.; Apicella, M.; Nauseef, W. M. *J. Immunol.* **1999**, *163*, 6732−6740. (b) Johansson, A.; Jesaitis, A. J.; Lundqvist, H.; Magnusson, K.-E.; Sjölin, C.; Karlsson, A.; Dahlgren, C. *Cell. Immunol.* **1995**, *161*, 61−71.

(19) (a) Jesaitis, A. J.; Buescher, E. S.; Harrison, D.; Quinn, M. T.; Parkos, C. A.; Livesey, S.; Linner, J. *J. Clin. Invest.* **1991**, *85*, 821−835. (b) Ginsel, L. A.; Onderwater, J. J. M.; Fransen, J. A. M.; Verhoeven, A. J.; Roos, D. *Blood* **1990**, *76*, 2105−2116.

(20) Jamin, N.; Dumas, P.; Moncuit, J.; Fridman, W.-H.; Teillaud, J.-L.; Carr, G. L.; Williams, G. P. *Proc. Natl. Acad. Sci. U.S.A.* **1998**, *95*, 4837−4840.

(21) For recent examples, see: (a) Uzunbajakava, N.; Lenferink, A.; Kraan, Y.; Volokhina, E.; Vrensen, G.; Greve, J.; Otto, C. *Biophys. J.* **2003**, *84*, 3968−3981. (b) Wood, B. R.; Langford, S. J.; Cooke, B. M.; Glenister, F. K.; Lim, J.; McNaughton, D. *FEBS Lett.* **2003**, *554*, 247−252. (c) Krafft, C.; Knetschke, T.; Siegner, A.; Funk, R. H. W.; Salzer, R. *Vib. Spectrosc.* **2003**, *32*, 75−83.

(22) For recent overviews, see: (a) Cheng, J.-X.; Xie, X. S. *J. Phys. Chem. B* **2004**, *108*, 827−840. (b) Holtom, G. R.; Thrall, B. D.; Chin, B.-Y.; Wiley: H. S.; Colson, S. D. *Traffic* **2001**, *2*, 781−788.

(23) Nan, X.; Cheng, J.-X.; Xie, X. S. *J. Lipid Res.* **2003**, *44*, 2202−2208.

(24) Van Manen, H.-J.; Uzunbajakava, N.; Van Bruggen, R.; Roos, D.; Otto, C. *J. Am. Chem. Soc.* **2003**, *125*, 12112−12113.

(25) Yazdanbakhsh, M.; Eckmann, C. M.; Koenderman, L.; Verhoeven, A. J.; Roos, D. *Blood* **1987**, *70*, 379−383.

(26) Sijtsema, N. M.; Otto, C.; Segers-Nolten, G. M. J.; Verhoeven, A. J.; Greve, J. *Biophys. J.* **1998**, *74*, 3250−3255.

(27) De Grauw, C. J.; Sijtsema, N. M.; Otto, C.; Greve, J. *J. Microsc.* **1997**, *188*, 273−279.

(28) See also: Schmidt, M.; Rajagopal, S.; Ren, Z.; Moffat, K. *Biophys. J.* **2002**, *84*, 2112−2129.

(29) Golub, G. H.; Van Loan, C. F. *Matrix Computations*; North Oxford Academic Publishing: Oxford, 1983.

(30) Haq, I.; Chowdhry, B. Z.; Chaires, J. B. *Eur. Biophys. J.* **1997**, *26*, 419−426.

(31) Puppels, G. J.; Olminkhof, J. H. F.; Segers-Nolten, G. M. J.; Otto, C.; De Mul, F. F. M.; Greve, J. *Exp. Cell. Res.* **1991**, *195*, 361−367.

(32) (a) Omberg, K. M.; Osborn, J. C.; Zhang, S. L.; Freyer, J. P.; Mourant, J. R.; Schoonover, J. R. *Appl. Spectrosc.* **2002**, *56*, 813−819. (b) Notingher, I.; Verrier, S.; Haque, S.; Polak, J. M.; Hench, L. L. *Biopolymers* **2003**, *72*, 230−240.

(33) Woodman, R. C.; Ruedi, J. M.; Jesaitis, A. J.; Okamura, N.; Quinn, M. T.; Smith, R. M.; Curnutte, J. T.; Babior, B. M. *J. Clin. Invest.* **1991**, *87*, 1345−1351.

(34) Borregaard, N.; Heiple, J. M.; Simons, E. R.; Clark, R. A. *J. Cell Biol.* **1983**, *97*, 52−61.

(35) (a) Brederoo, P.; Van der Meulen, J.; Mommaas-Kienhuis, A. M. *Cell Tissue Res.* **1983**, *234*, 469−496. (b) Rothwell, S. W.; Nath, J.; Wright, D. G. *J. Cell Biol.* **1989**, *108*, 2313−2326.

(36) Wever, R.; Plat, H. *Biochim. Biophys. Acta* **1981**, *661*, 235−239.

(37) (a) Kooter, I. M.; Moguilevsky, N.; Bollen, A.; Van der Veen, L. A.; Otto, C.; Dekker: H. L.; Wever, R. *J. Biol. Chem.* **1999**, *274*, 26794−26802. (b) Kooter, I. M.; Koehler, B. P.; Moguilevsky, N.; Bollen, A.; Wever, R.; Johnson, M. K. *J. Biol. Inorg. Chem.* **1999**, *4*, 684−691.

(38) (a) Gebhardt, C.; Heinemann, U. *Brain Res.* **1999**, *837*, 270−276. (b) Yuan, X. J.; Goldman, W. F.; Tod, M. L.; Rubin, L. J.; Blaustein, M. P. *Am. J. Physiol.* **1993**, *264*, L116−L123.

(39) For a related effect of sodium metabisulfite on fluorescence photobleaching in cells, see: Benson, D. M.; Bryan, J.; Plant, A. L.; Gotto, A. M.; Smith, L. C. *J. Cell Biol.* **1985**, *100*, 1309−1323.

(40) (a) Segal, A. W.; Dorling, J.; Coade, S. *J. Cell Biol.* **1980**, *85*, 42−59. (b) Borregaard, N.; Cowland, J. B. *Blood* **1997**, *89*, 3503−3521.

(41) English, D. In *The Neutrophils: New Outlook for Old Cells*; Gabrilovich, D. I., Ed.; Imperial College Press: London, 1999; Chapter 1.

(42) Gomperts, B. D.; Kramer, I. M.; Tatham, P. E. R. *Signal Transduction*; Elsevier Academic Press: San Diego, 2002; Chapter 9.

(43) (a) Segal, A. W.; Jones, O. T. G. *Biochem. Biophys. Res. Commun.* **1979**, *88*, 130−134. (b) Cross, A. R.; Higson, F. K.; Jones, O. T. G.; Harper, A. M.; Segal, A. W. *Biochem. J.* **1982**, *204*, 479−485.

(44) Calculated from the peak intensities of the 1362 (reduced cyt b_{558}) and the 1375 cm^{-1} (oxidized cyt b_{558}) bands.

Resonance Raman Imaging on Single Granulocytes

J. Phys. Chem. B, Vol. 108, No. 48, 2004 **18771**

(45) Determined from 50 randomly selected points inside the cell shown in Figure 5A.

(46) Demaurex, N.; Downey, G. P.; Waddell, T. K.; Grinstein, S. *J. Cell Biol.* **1996**, *133*, 1391−1402.

(47) The second basis vector (not shown) resembles the first basis vector, but it differs in the shape and intensity of the background.

(48) For an overview, see: Giembycz, M. A.; Lindsay, M. A. *Pharmacol. Rev.* **1999**, *51*, 213−339.

(49) Segal, A. W.; Garcia, R.; Goldstone, H.; Cross, A. R.; Jones, O. T. G. *Biochem. J.* **1981**, *196*, 363−367.

(50) Klebanoff, S. J.; Agosti, J. M.; Jorg, A.; Waltersdorph, A. M. *J. Immunol.* **1989**, *143*, 239−244.

(51) Salmaso, B. L. M.; Puppels, G. J.; Caspers, P. J.; Floris, R.; Wever, R.; Greve, J. *Biophys. J.* **1994**, *67*, 436−446.

(52) Spiro, T. G.; Strekas, T. C. *J. Am. Chem. Soc.* **1974**, *96*, 338−345.

(53) Van Manen, H.-J.; Otto, C. Unpublished results.